Shaping single walled nanotubes with an electron beam

A. Zobelli,[1,2,*] A. Gloter,[1] C. P. Ewels,[3] and C. Colliex[1]
[1]*Laboratoire de Physique des Solides, Université Paris-Sud, CNRS, UMR 8502, F-91405 Orsay Cedex, France*
[2]*Technische Universität Dresden, Institüt für Physikalische Chemie und Elektrochemie, D-1062 Dresden, Germany*
[3]*Université de Nantes, Nantes Atlantique Universités, CNRS, Institut des Matériaux Jean Rouxel (IMN), UMR6502, BP32229, F-44322 Nantes Cedex 3, France*
(Received 19 September 2007; published 15 January 2008)

We show that electron irradiation in a dedicated scanning transmission microscope can be used as a nano-electron-lithography technique allowing the controlled reshaping of single walled carbon and boron nitride nanotubes. The required irradiation conditions have been optimized on the basis of total knock-on cross sections calculated within density functional based methods. It is then possible to induce morphological modifications, such as a local change of the tube chirality, by sequentially removing several tens of atoms with a nanometrical spatial resolution. We show that electron beam heating effects are limited. Thus, electron beam induced vacancy migration and nucleation might be excluded. These irradiation techniques could open new opportunities for nanoengineering a large variety of nanostructured materials.

DOI: 10.1103/PhysRevB.77.045410 PACS number(s): 61.46.Fg, 61.80.Fe, 61.80.Az, 61.72.Ff

I. INTRODUCTION

Irradiation of nanotubes is now a widespread issue which is primarily encountered within two contexts.

Firstly, nanotube irradiation with different energetic particles, such as γ rays,[1,2] electrons,[3,4] protons,[5,6] and ions,[7] can be deliberately used to alter the chemical, mechanical, and electronic properties of the tubes. For example Kis *et al.*[4] have shown a strong stiffening of bundles of carbon nanotubes after electron irradiation. Another example can be found in the work of Gómez-Navarro *et al.*[7] where Ar^+ ion bombardment of carbon nanotubes provoked a dramatic increase in the tube electrical resistivity.

Secondly, irradiation is also an unavoidable side effect occurring when highly energetic particles are used to investigate structural and spectroscopic properties of the tubes. This is of particular importance for transmission electron microscopy (TEM) which allows the observation of individual defects on nanotubes.[8–10] Meanwhile, the electron beam might also damage the nanotube structure. This eventually leads to extended wavy morphologies and ultimately complete tube amorphization.[11] Recently, Yuzvinsky *et al.*[12] demonstrated that the crystallinity of the tube can be preserved through thermal treatments during the TEM observation.

A more limited number of studies have tried to use the focusing properties of electrons to locally modify the nanotube structure. Li and Banhart[13] have demonstrated that focusing electron probes on multiwalled carbon nanotubes (MWCNTs) can bend the tubes or locally produce carbon onions from the tubes walls. Yuzwinsky *et al.*[14] have demonstrated that MWCNTs can be cut with a scanning electron microscope even at low electron voltage when a degraded vacuum is present.

Nonetheless, the technological potential of electron irradiation of nanotubes is far from being realized. This is primarily because, until now, theory was not able to quantitatively predict the expected defect structures as a function of the irradiation parameters, and experiments were not performed with sufficient spatial control.

In the current paper, we present a fundamental improvement in the irradiation techniques, optimizing irradiation conditions on the basis of calculated knock-on cross sections.[15] We show that dislocations of a few nanometers in length, corresponding to the removal of a few tens of atoms, can be obtained with nanometrical accuracy using subnanometrical focused probes in a dedicated scanning transmission electron microscope (STEM). Experimental shaping of single walled carbon and boron nitride nanotubes are then obtained, demonstrating that chiralities of the tube can be locally changed with nanometric spatial control.

II. KNOCK-ON CROSS SECTIONS OF DEFECTIVE NANOTUBES

Under electron irradiation, defects appear in single walled nanotubes mainly due to direct (quasielastic scattering) collisions between the relativistic electrons of the beam and the atomic nucleus. Removal of the atom is thus obtained through the so-called knock-on effect. In Ref. 15, the theory of irradiation processes is detailed and total knock-on cross sections are presented for perfect carbon and boron nitride nanotubes as a function of the energy of the incident beam for different emission sites around the tube circumference. We note, however, that these calculations were only performed for the creation probability of single isolated vacancies. Under electron irradiation, it has been reported that nanotubes show kinks or extended defect formation and these structures are interpreted as the creation of dislocations by sequential removal of a series of adjacent atoms. The preferential creation of dislocation lines versus a random distribution of single vacancies has been explained by a laddering mechanism: once a primary vacancy is formed, the emission probability for one of the atoms neighboring the vacancy is higher than for atoms in a perfect graphitic environment.[8,16–19] This process has been proposed on the basis of lower vacancy formation energies at atom sites neighboring a preexisting vacancy or located at the ends of a dislocation line. However, vacancy formation energies are only indirectly related to emission probabilities of atoms. Consequently, we have derived the total knock-on cross section for atoms emitted during the first steps of the dislocation

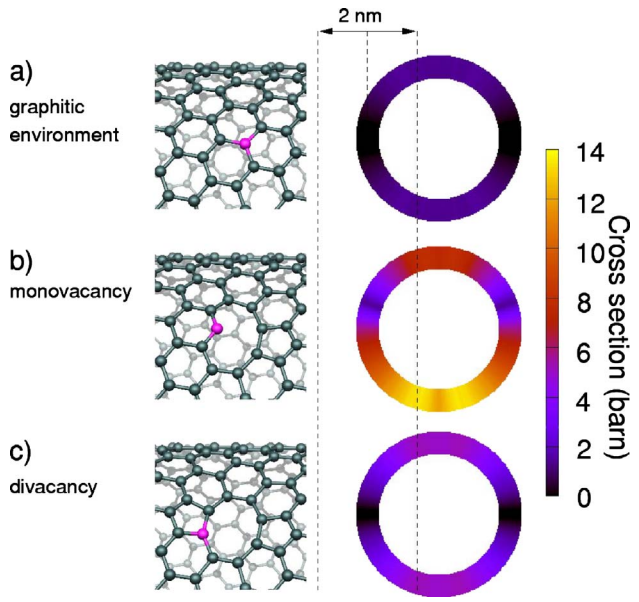

FIG. 1. (Color online) Right part of the figure: total knock-on cross section as a function of the position on a tube section (a) of an atom in a perfect graphitic environment, (b) of a double coordinated atom neighboring a monovacancy, and (c) of an atom neighboring a divacancy. The beam incidence direction is aligned along the figure's vertical axis. The two vertical dashed lines represent the irradiated zone used to obtain experimental tube shaping. Left section: structures of the targeted nanotubes. Emitted atoms are marked in magenta.

propagation process. As previously reported,[15] our knock-on cross section calculation involves the derivation of the emission energy threshold through extended density functional based molecular dynamics simulations[15,20] and a successive integration of the Mott cross section over the allowed emission solid angle.

Figure 1 shows the knock-on cross section for, respectively, an atom in a perfect graphitic environment (a), a doubly coordinated atom neighboring a monovacancy (b), and an atom neighboring a divacancy (c). The right side graphs represent the transversal section of the nanotube where the color scale refers to the total knock-on cross section at that location for each of these atom types. Figure 1 presents the results obtained for an electron beam energy 20 keV above the threshold energy at which defects can be generated; experimental tube shaping has been done at this corresponding energy.

For a perfect carbon nanotube [Fig. 1(a)], a strong angular dependence on the emission probability is obtained. The cross section decreases with increasing angle between the beam incidence direction and the normal to the tube, and a forbidden emission region appears corresponding to the side walls of the tube. Once a first vacancy is generated, a pentagonal ring appears with the reconstruction of a C-C bond between two vacancy neighbors. The third neighboring atom remains with one dangling bond and shifts slightly radially outward. For this lower coordinated atom, knock-on cross sections are almost 1 order of magnitude higher than for an atom in a perfect tube [Fig. 1(b)]: on tube regions perpendicular to the electron beam, a maximum cross section of 13.4 b is obtained, while a perfect graphitic environment shows only cross sections of about 1.4 b. The asymmetry between the upper and lower parts of the tube in Fig. 1(b) is due to the outward movement of the doubly coordinated atom, which makes emission into the tube cavity more difficult. Nanotubes with different chiralities, on which the vacancy symmetry plane is oriented in different directions, would have slightly different maps of the total cross section.

After removal of one atom close to a preexisting vacancy, the nanotube relaxes with the formation of a large divacancy and the creation of two pentagonal rings. The cross section map reported in Fig. 1(c) corresponds to the emission of one of the atoms neighboring a divacancy. A maximal cross section of 5.2 b is found in the tube sections normal to the beam incident direction, showing a partial stabilization of the atom compared to the previous case. With further knock-on events, odd and even numbers of vacancies are sequentially obtained and form a dislocation line. For odd numbers of vacancies, the tube relaxes similarly to the monovacancy case, with the appearance of a pentagonal ring and a doubly coordinated atom. This is equivalent to a basal plane dislocation terminating in the shuffle plane. Analogously, the removal of an even number of atoms gives a structure with ends topologically equivalent to a divacancy, i.e., two pentagonal rings at the ends of the dislocation line. In this case, both dislocation cores terminate in the glide plane. Due to these morphological similarities, we expect the emission knock-on cross section for the odd and even cases to correspond to values close to those obtained for the monovacancy and divacancy, respectively.

The high emission probabilities for atoms at the two ends of a dislocation compared to atoms in a perfect graphitic environment support the existence of preferential sites for atomic emission that provoke the propagation of dislocation lines under electron irradiation through a laddering mechanism. One can see direct experimental confirmation of this theoretical model in the TEM movies presented in a recent work of Suenaga *et al.* (Ref. 10, supporting materials movie S4). The movie shows an initial short dislocation which ends at two kinks on the tube side walls. During the acquisition time, the two kinks move far from each other with a related tube diameter reduction. This behavior corresponds to atom emission under irradiation at the two ends of the dislocation loop, which propagates the dislocation along the tube axis.

While Fig. 1 only shows the knock-on cross section at the experimental electron voltage used in the following section, calculations have been done for a large range of voltage. The map of the total knock-on cross section for atoms in a perfect carbon nanotube as a function of the incident electron energy and the position of atoms around the tube circumference has been already presented in Ref. 15. We report here analogous maps for the emission of carbon atoms in defective nanotubes in Fig. 2 (atom neighboring a monovacancy) and Fig. 3 (atom neighboring a bivacancy). The polar coordinate represents the atom position within the tube circumference, the radial coordinates represent the knock-on cross section expressed in barn, and the different curves refer to different incident electron beam energies. With respect to the experimental setup, the incoming electron direction is from the top to the bottom ($\alpha=0°$).

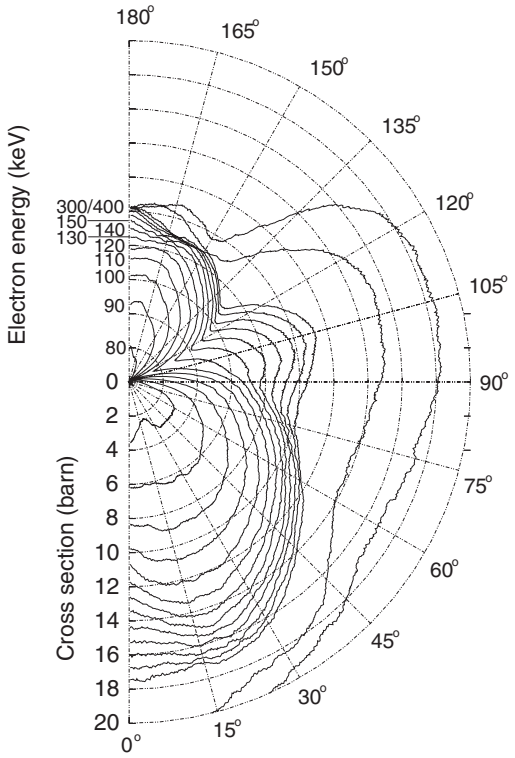

FIG. 2. Total knock-on cross section for a double coordinated atom neighboring a monovacancy as a function of its position α around the tube circumference.

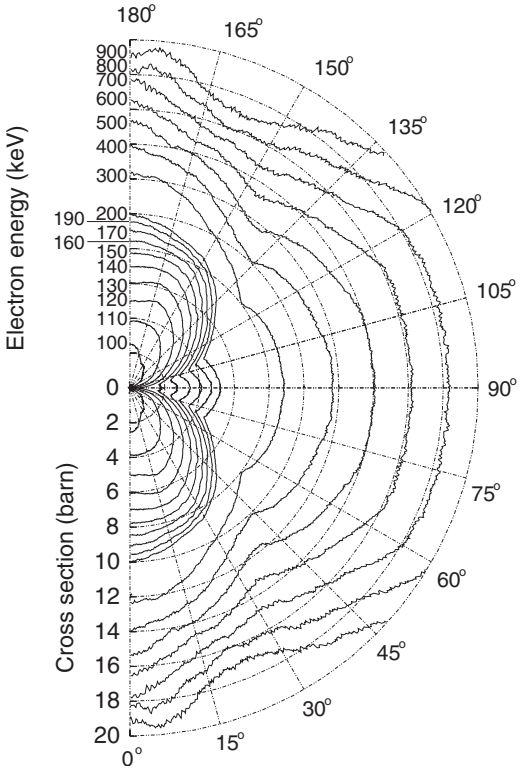

FIG. 3. Total knock-on cross section for a carbon atom neighboring a divacancy as a function of its position α around the tube circumference.

III. SINGLE WALLED CARBON NANOTUBE ELECTRON IRRADIATION

Experimental conditions for single walled carbon nanotube irradiation have been optimized on the basis of the calculated total knock-on cross sections in order to obtain tube shaping capability. In Fig. 4, such a shaping of a single walled carbon nanotube is obtained by successive cycles of local electron irradiation. Five extended kinks have been obtained sequentially, on alternating sides of the tube. To obtain such controlled irradiation, we select illuminated area, electron beam current density, and electron beam energy in order

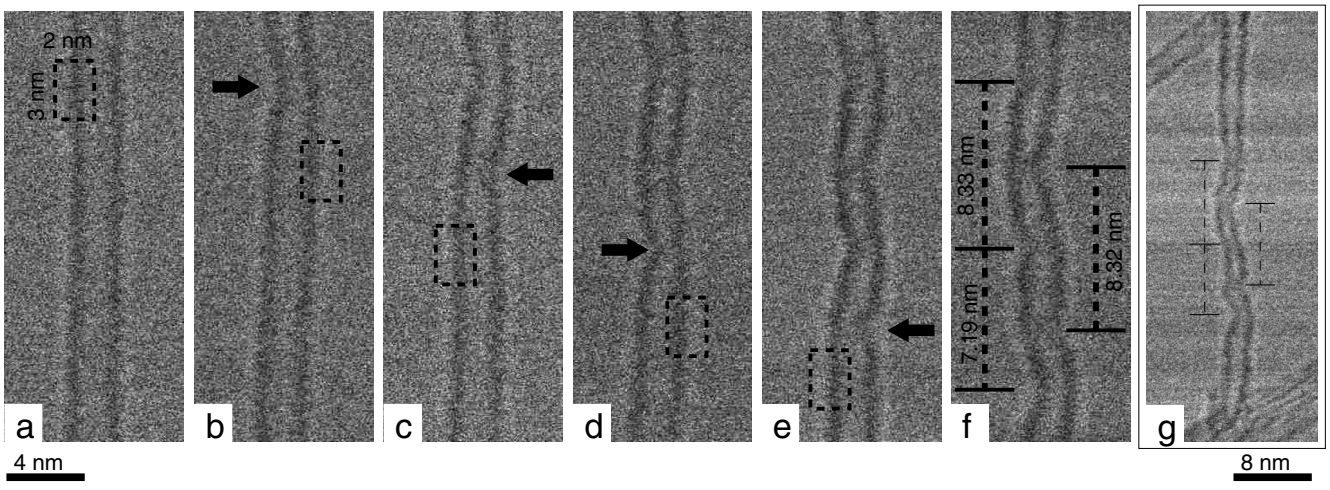

FIG. 4. Local electron irradiation of a single walled carbon nanotube. Irradiation zones of 2×3 nm^2 are represented by the dashed rectangles. (a) Original tube with a diameter of 2.4 nm and an apparent perfect crystallinity. (b) After the first irradiation cycle, the tube shows a kink associated with a slight bending (black arrow) in direct correspondence with the chosen irradiated zone. [(c)–(f)] Similar defective structures appear after each irradiation cycle, as noted with arrows. (g) Final structure observed at a lower magnification, demonstrating that the non-irradiated zones at the two extreme parts of the tubes remain unaltered.

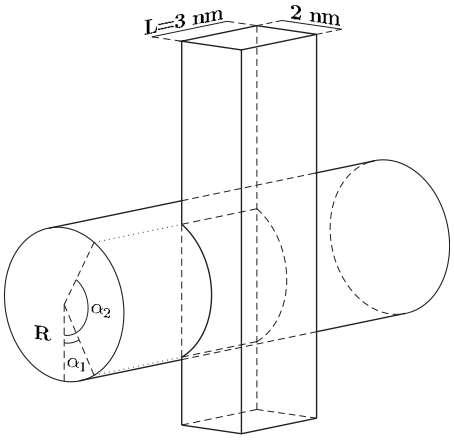

FIG. 5. Schematic representation of the irradiation geometry of a nanotube. The electron beam incidence direction is orthogonal to the tube axis.

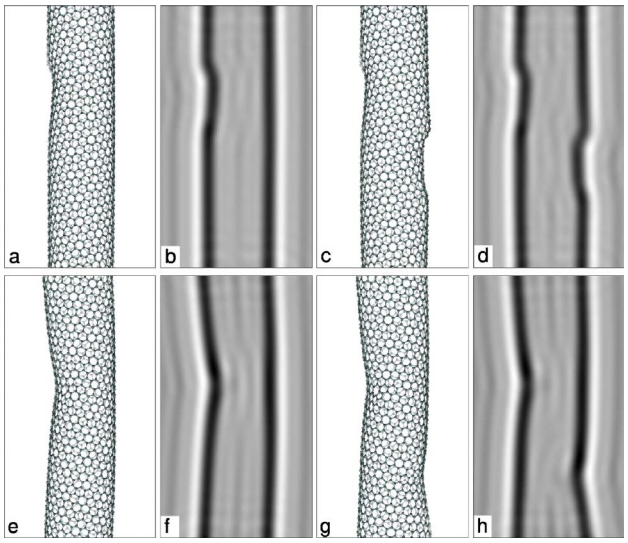

FIG. 6. (Color online) Relaxed structure and respective STEM bright field simulated images for different dislocation lines in a (20,5) single walled carbon nanotube. Structures (a) and (e) correspond to a single dislocation line made of 12 missing atoms with different orientations. Structures (c) and (g) correspond to the presence of two dislocations in the tube.

to have a low atom ejection rate during the exposure time. Irradiation cycles were performed using an electron beam energy of 100 keV (roughly 20 keV above threshold voltage[21]), an electron current of ~140 pA, and exposure times of 60 s. The beam convergence half-angle has been set to about 7.5 mrad, which corresponds to an electron probe diameter of 0.8 nm. Five irradiation cycles were performed, choosing sequential irradiation zones on alternating sides of the tube at about 4 nm spacing along the tube axis. The scanning regions, represented in Fig. 4 by the dashed rectangles, are limited to a 2×3 nm^2 area and partially illuminate the external section of the tube walls. As shown in Fig. 1, atoms located on these sectors of the tube have the lowest total knock-on cross section and, therefore, a better control of the irradiation process can be obtained using longer exposure times.

TEM experiments are usually performed with nanotubes deposited onto a lacey carbon grid placed perpendicular to the TEM axis and, thus, electron irradiation is then primarily performed in a nontilted geometry where the tube axis lies perpendicular to the direction of the electron beam (see Fig. 5). In this configuration, the position of the atoms around the tube circumference can be identified using the angle α defined by the direction of incidence of the electron and the local normal to the tube wall. The number of events, N, that occur at a position α on the tube for an irradiation time t can be obtained by

$$N = jRLt\int_{\alpha_1}^{\alpha_2} \sigma(\alpha)\rho|\cos(\alpha)|d\alpha,$$

where ρ is the atom density of a graphene plane, j is the current density, R is the tube radius, and L is the illuminated length along the tube axis. ρ represents then the atom surface density. The intersection between the electron beam irradiation zone and the nanotube is defined by the two integration limit polar angles α_1 and α_2. In the experimental setup previously described, the operating current density in the microscope was fixed at about 150×10^{28} e^-/s m^2. We consider an atom surface density of 9.68 atoms/nm^2 for a graphene plane and an effective illumination area defined by an illuminated length $L=3$ nm and the two polar angles $\alpha_1=60°$ and $\alpha_2=120°$. Under these experimental conditions, a total number of 2.7 vacancies is generated during an exposure time of $t=60$ s.

These primary vacancies act as seeds for subsequent atom removal and, finally, for the creation of dislocation lines. By combining the higher knock-on cross sections for additional vacancies created adjacent to the first vacancy sites with the low concentration of primary vacancies, an overall emission of a few tens of atoms from the tube is estimated during each irradiation event. In Appendix B, we will estimate the temperature of the nanotubes under the irradiation and demonstrate that the electron beam heating effects are limited. In addition, thermal vacancy migration or spontaneous emission of atoms is unlikely at room temperature for C and BN systems.[20,22] This is the reason why the tube shaping is stable and why kinks are only obtained in the regions where the electron irradiation conditions were optimized for.

The sequential removal of atoms along a line introduces pentagon-heptagon defect pair and changes locally the tube chirality from (m,n) to $(m\pm 1,n\mp 1)$. For particular pairs of the Hamada indices m,n, the dislocation line can then change locally the electronic character of the tubes from semiconductor to metallic and vice versa.[23,24]

The introduction of these dislocation lines produces a shortening of the tube whose length corresponds in a first approximation to the component of the Burgers vector along the tube axis. The bending of the tube visible in the microscopy images is then associated with shrinkage of one of the tube sides, and its magnitude depends on the orientation of the dislocation. This behavior is illustrated by the example of Fig. 6. Considering a (20,5) chiral carbon nanotube, whose

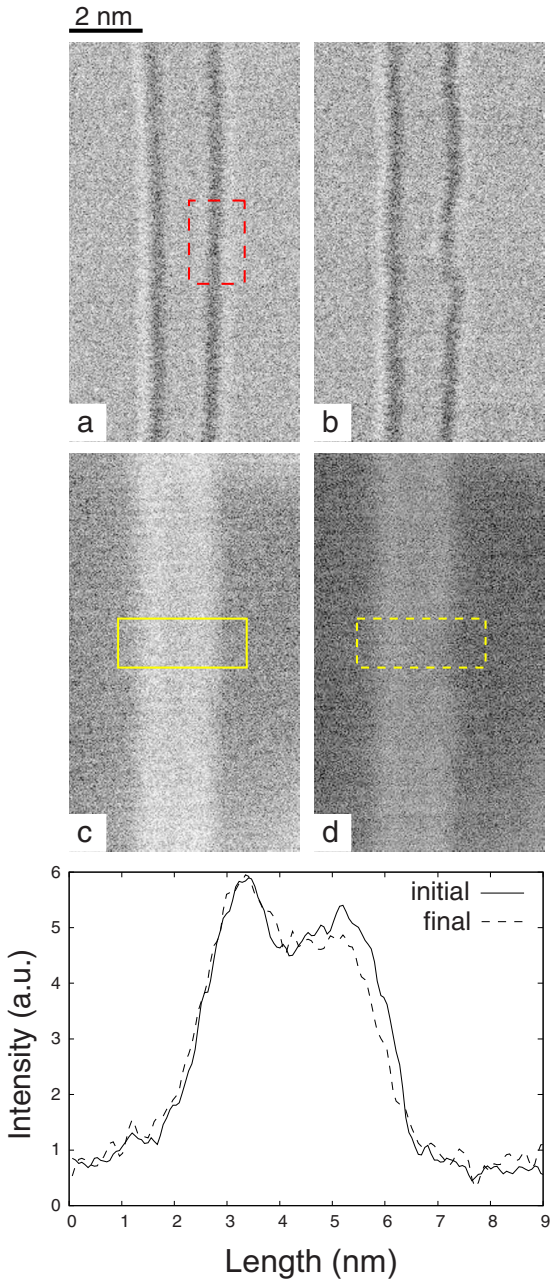

FIG. 7. (Color online) Localized irradiation of a single walled BN nanotube. [(a) and (b)] Experimental STEM bright field images before and after the irradiation cycle of the nanotube. [(c) and (d)] Corresponding STEM dark field images before and after the irradiation cycle. Lower part of the figure: STEM dark field profile of the nanotube showing tube thinning on the right. From the difference of the profile integrals, it can be estimated that around 4% of the atoms have been sputtered.

diameter is compatible with the tube of Fig. 4, the tube structures with differently oriented dislocation lines have been relaxed by density functional tight binding (DFTB) and microscope images have been simulated. In Fig. 6(a), the removal of 12 atoms along a direction of 10.95° with respect to the tube axis does not produce any visible bending of the tube [Fig. 6(b)] but two separated kinks are clearly visible in the left wall. When two dislocation lines are present in the

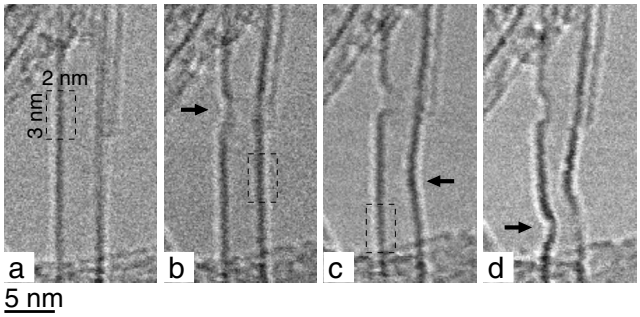

FIG. 8. Shape modification of a BN nanotube under localized irradiation.

tube, with a separation of several nanometers along the tube axis, the result is quite similar. No substantial bending of the tube is obtained and the dislocations are only visible though extended defects on the right and left parts of the tube [Figs. 6(c) and 6(d)]. Removing the same number of atoms along a different direction of 79.05°, closer to the normal of the tube axis, gives a larger shortening of one side of the tube, which corresponds after relaxation to a bending of the tubular structure [Fig. 6(e)]. The simulated microscope images with one or two dislocation lines [Figs. 6(d) and 6(f)] reproduce well the behavior observed in the experimentally irradiated nanotubes [Figs. 4(b) and 4(c)], demonstrating that a few tens of atoms have been removed by the electron beam.

Similar irradiation conditions can be used in the shaping of single walled boron nitride nanotubes. Compared to carbon irradiation, defects in BN nanotubes appear at lower irradiation energies.[15] An irradiation beam energy of 80 keV, slightly above the electron irradiation energy threshold, has thus been chosen in order to control the irradiation damage.

Figure 7(a) presents a single walled boron nitride nanotube before irradiation. Figure 7(b) is taken after 60 s of irradiation, the dashed red rectangle in Fig. 7(a) representing the 2×3 nm^2 irradiated area. After the irradiation cycle, the tube diameter appears locally reduced in the bright field image and two kinks appear in the tube walls.

STEM annular dark field images give a direct correlation between the local intensity of the image and the local atomic density of the sample and can be used to quantify the loss of atoms [Figs. 7(c) and 7(d)]. The intensity profiles obtained across the tube before and after the irradiation are legible in the lower part of Fig. 7. After the irradiation cycle is applied to the right side of the wall, the profile shows a decrease in intensity and the tube diameter shrinks from 2.0 to 1.8 nm. With the profile integral being proportional to the number of atoms, an estimate of around 4% of the atoms, corresponding to a few tens of atoms, has been sputtered from the tube during the irradiation cycle. This value is in agreement with the theoretically expected numbers of vacancies.

Similarly to single walled carbon nanotubes, it is possible to repeat the irradiation procedure in different sections of a BN tube in order to reshape the nanotube with a nanometric periodicity (Fig. 8).

Figure 9 shows that, as for carbon nanotubes, local irradiation can produce a relevant bending of the tube. However, this bending effect seems to be less common than for carbon

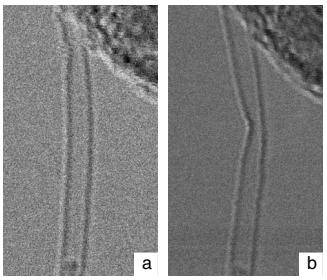

FIG. 9. BN nanotube bending obtained through localized electron irradiation.

nanotubes. We propose that for BN nanotubes, this effect is also related to the shortening of one of the tube wall sides.

IV. CONCLUSIONS

In the present paper, we have derived, through extended DFTB based simulations, the total knock-on cross section for atoms neighboring defects in single walled carbon nanotubes. These values have been used as a guideline for the optimization of irradiation conditions in TEM experiments.

The experiments presented give indications for a "nano-electron-lithography" of single walled nanotubes, a top down approach to locally control their nanostructures. In particular, we demonstrate that electron irradiation optimized on the basis of knock-on cross sections calculated in a density functional based framework can be used to remove a series of a few tens of atoms in a periodic area along the tube axis.

The sequential removal of atom lines results to local changes of the tube chirality which, in particular cases, could result to a modification of the electronic properties of the tube. It is currently impossible to have a precise control of the chiral index change since electron microscopes have not yet attained the capability of knocking out a specifically targeted atom. Nevertheless, the knock-on cross sections presented here can be also used as a "guide book" for that purpose, a unique way to generate a wide variety of carbon-based quasi-one-dimensional conductive systems, from quantum wells to nanodiodes.

ACKNOWLEDGMENTS

We would like to thank R. Arenal de la Concha and A. Loiseau for having kindly provided the BN nanotubes samples and M. Tencé for the development in the STEM probe scanning system. A.Z. acknowledges the New Fullerene-like materials network (Contract No. HPRNCT-2002-00209) and the Enabling Science and Technology for European Electron Microscopy network (Contract No. ESTEEM-0260019) for financial support.

APPENDIX A: METHODS

1. Scanning transmission electron microscope

Experiments have been performed in a VG-HB501 STEM equipped with a tungsten cold field-emission gun. The vacuum in the vicinity of the sample was around 5×10^{-8} torr and has been obtained with an oil-free pumping system. High mechanical sample stability was obtained by a top-entry sample holder system. The beam convergence half-angle was set to about 7.5 mrad and the used pole piece has a spherical aberration of around 3.1 mm. For voltage energy of 100 keV, it corresponds to the formation of an electron probe of around 0.8 nm in diameter at the sample surface. Electron probe sizes were slightly degraded when lower voltages such as 60 or 80 keV were used. Bright field (BF) images have been obtained with a collection semiangle of 1.25 mrad and dark field (DF) images have been obtained with collection angle between 25 and 200 mrad. Irradiation conditions to obtain tube shaping are discussed in the body text. For BF-DF imaging, the acquisition time was limited to 1–2 s and, when needed beam, blanking was used before the sample in order to limit the electron irradiation required to image the nanotube. In such conditions, the statistical creations of vacancies during the imaging procedure of the tube were calculated to be around 0.1 over the full section of the imaged nanotube. Electron beam currents have been calibrated by a direct measurement of the current inside the drift tube of an electron energy loss spectroscopy (EELS) spectrometer using a Keithley picoamperometer. Single walled carbon nanotubes have been synthesized by the chemical deposition process and are of commercial origin (Thomas Swan & Co. Ltd). Boron nitride nanotube synthesis is described elsewhere[25] and tubes have been provided to us by Arenal de la Concha and Loiseau (LEM-Onera, France).

2. Calculations

Knock-on cross sections have been calculated in a similar manner as described in detail in Ref. 15. Atom emission occurs for scattering angles where the energy transferred to the nucleus is higher than a certain escaping energy. Firstly, maps of the emission energy threshold as a function of the emission angle have been obtained through extended density functional based molecular dynamics simulations.[15,20] Molecular dynamics has been performed using the DFTB method simulating the local environment of carbon nanotubes by a planar graphene sheet. Details of the DFTB parameters can also be found in Ref. 15. The total knock-on cross sections have then been calculated by integration of the Mott cross section[26–28] for the set of angles satisfying the emission conditions.

In the microscopy image simulations, section structural optimizations have been conducted in the framework of the density functional tight binding theory[29,30] using the DFTB+ code.[31] We have considered a (20,5) single walled carbon nanotube with a tube diameter of 1.8 nm. In order to allow the bending of the tube, calculations have been performed in a cluster mode using models containing up to 1800 atoms. Dangling bonds at open caps have been saturated by addition of hydrogen atoms.

Microscopy simulated images have been obtained using the multislice simulation method included in the TEMSIM packages.[32]

APPENDIX B: ELECTRON BEAM NANOTUBE HEATING

In a transmission electron microscopy, inelastic collisions between the electrons of the beam and the electrons bonded to atoms lead to a significant energy transfer which is converted to a local heating of the sample.[33,34] Direct phonon excitations have an extremely low cross section and this process has a minimal effect on the irradiation induced heating of the sample. Thermal heating occurs then mostly through deexcitation of plasmon modes into phonon modes. Without entering into details of the different processes involved in inelastic scattering, we can consider more simply the energy transferred (E_T) each second to the sample which is successively converted into internal thermal energy. This quantity can be evaluated as

$$E_T = I\langle E\rangle \frac{t}{\lambda}, \tag{B1}$$

where I is the incident beam current density, λ is the average mean free path for all inelastic scattering, and t is the sample thickness. The term $\langle E\rangle$ is the average energy loss (expressed in eV) per inelastic collision and it can be estimated as

$$\langle E\rangle = \int EA(E)dE \Big/ \int A(E)dE, \tag{B2}$$

where $A(E)$ is the intensity of the energy loss spectrum at an energy E which can be experimentally obtained from a measured EELS spectrum. The quantity t/λ represents the probability that one electron would transfer an average energy $\langle E\rangle$ into the irradiated zone. This quantity can be experimentally evaluated from

$$\frac{t}{\lambda} = \log \frac{\int A(E)dE}{\int_{\text{zlp}} A(E)dE}, \tag{B3}$$

where in the logarithm, it appears as the ratio between the intensity of the whole energy loss spectrum and the intensity of the zero loss peak. From the works of Taverna *et al.*[35] on plasmons in single walled carbon nanotubes and Arenal *et al.*[36] on plasmons in BN nanotubes, we have estimated t/λ to be equal to 0.02.

For calculating the effective temperature rising in the sample, we also have to consider the effect of thermal dispersion into the energetic balance. Considering a total beam current I and a beam diameter d, the equation relating heating and emission can be expressed by[34]

$$I\langle E\rangle \frac{t}{\lambda} = \kappa S \frac{T - T_0}{L} + \pi \frac{d^2}{2} \sigma(\varepsilon T^4 - \varepsilon_0 T_0^4). \tag{B4}$$

In this equation, the final temperature of the sample is indicated as T. The first addendum of the second term represents the dispersion of heating due to linear conduction over a distance L in a material of thermal conductivity κ, section S, and thermostat temperature T_0. The second addendum considers the radiation of the sample where $\sigma = 5.67 \times 10^{-8}$ W m^{-2} K^{-4} is Stefan's constant, ε is the emissivity of the specimen, and ε_0 is the emissivity of the environment.

It has been demonstrated that carbon nanotubes have an exceptional thermal conductivity as high as $\kappa = 3500$ W/m K.[37] We can evaluate the effect of irradiation thermal heating considering an electron beam current I around 10 nA and a spot size diameter $d = 1$ nm. We chose a tube section $S = 1$ nm^2 and we consider the thermal conduction over the length of the scanned area $L = 3$ nm. The sample emissivity can be estimated in $\varepsilon = 0.98$, which corresponds to the emissivity of graphite, and the environment emissivity is commonly set equal to $\varepsilon_0 = 0.5$.[34] Integrating these experimental conditions into Eq. (B4), we obtain that the electron beam produces a temperature rise of the order of magnitude of 10^{-3} K.

It has been experimentally shown that vacancy in graphite can be annealed at a temperature of around 520 K. In the case of BN sheets, in a precedent work, we demonstrated that vacancy migration occurs at a much higher temperature, estimated above 800 K.[22] Subsequently, the extremely limited thermal effect produced by electron irradiation cannot be responsible for vacancy migration in the experiments conducted at room temperature.

*zobelli@lps.u-psud.fr

[1] M. Hulman, V. Skákálova, S. Roth, and H. Kuzmany, J. Appl. Phys. **98**, 024311 (2005).
[2] V. Skákálova, U. Dettlaff-Weglikowska, and S. Roth, Diamond Relat. Mater. **13**, 296 (2004).
[3] F. Beuneu, C. l'Huillier, J. P. Salvetat, J. M. Bonard, and L. Forro, Phys. Rev. B **59**, 5945 (1999).
[4] A. Kis, G. Csanyi, J. Salvetat, T. Lee, E. Couteau, A. Kulik, W. Benoit, J. Brugger, and L. Forró, Nat. Mater. **3**, 153 (2004).
[5] V. Basiuk, K. Kobayashi, T. Kaneko, Y. Negishi, E. Basiuk, and J. Saniger-Blesa, Nano Lett. **2**, 789 (2002).
[6] B. Khare, M. Meyyappan, M. Moore, P. Wilhite, H. Imanaka, and B. Chen, Nano Lett. **3**, 643 (2003).
[7] C. Gómez-Navarro, P. de Pablo, J. Gómez-Herrero, B. Biel, F. Garcia-Vidal, A. Rubio, and F. Flores, Nat. Mater. **4**, 534 (2005).
[8] A. Zobelli, C. Ewels, A. Gloter, G. Seifert, O. Stephan, S. Csillag, and C. Colliex, Nano Lett. **6**, 1955 (2006).
[9] A. Hashimoto, K. Suenaga, A. Gloter, K. Urita, and S. Iijima, Nature (London) **430**, 870 (2004).
[10] K. Suenaga, H. Wakabayashi, M. Koshino, Y. Sato, K. Urita, and S. Iijima, Nat. Nanotechnol. **2**, 358 (2007).
[11] P. Ajayan, C. Colliex, P. Bernier, and J. Lambert, Microsc. Microanal. Microstruct. **4**, 501 (1993).
[12] T. Yuzvinsky, W. Mickelson, S. Aloni, G. Begtrup, A. Kis, and A. Zettl, Nano Lett. **6**, 2718 (2006).
[13] J. Li and F. Banhart, Nano Lett. **4**, 1143 (2004).
[14] T. Yuzwinsky, A. Fennimore, W. Mickelson, C. Esquivias, and A.

Zettl, Appl. Phys. Lett. **86**, 053109 (2005).
[15] A. Zobelli, A. Gloter, C. P. Ewels, G. Seifert, and C. Colliex, Phys. Rev. B **75**, 245402 (2007).
[16] K. Niwase, Mater. Sci. Eng., A **400**, 101 (2005).
[17] F. Ding, K. Jiao, M. Wu, and B. I. Yakobson, Phys. Rev. Lett. **98**, 075503 (2007).
[18] F. Ding, K. Jiao, M. Wu, and B. Yakobson, Nano Lett. **7**, 681 (2007).
[19] J. Kotakoski, A. V. Krasheninnikov, and K. Nordlund, Phys. Rev. B **74**, 245420 (2006).
[20] A. V. Krasheninnikov, F. Banhart, J. X. Li, A. S. Foster, and R. M. Nieminen, Phys. Rev. B **72**, 125428 (2005).
[21] B. Smith and D. Luzzi, J. Appl. Phys. **90**, 3509 (2001).
[22] A. Zobelli, C. P. Ewels, A. Gloter, and G. Seifert, Phys. Rev. B **75**, 094104 (2007).
[23] L. Chico, V. H. Crespi, L. X. Benedict, S. G. Louie, and M. L. Cohen, Phys. Rev. Lett. **76**, 971 (1996).
[24] L. Ruppalt and J. Lyding, Small **3**, 280 (2007).
[25] R. S. Lee, J. Gavillet, M. Lamy de la Chapelle, A. Loiseau, J.-L. Cochon, D. Pigache, J. Thibault, and F. Willaime, Phys. Rev. B **64**, 121405(R) (2001).
[26] N. Mott, Proc. R. Soc. London, Ser. A **124**, 425 (1929).
[27] N. Mott, Proc. R. Soc. London, Ser. A **135**, 429 (1932).
[28] W. McKinsley and H. Feshbach, Phys. Rev. **74**, 1759 (1948).
[29] D. Porezag, T. Frauenheim, T. Kohler, G. Seifert, and R. Kaschner, Phys. Rev. B **51**, 12947 (1995).
[30] G. Seifert, D. Porezag, and T. Frauenheim, Int. J. Quantum Chem. **58**, 185 (1996).
[31] B. Aradi, B. Hourahine, C. Koehler, and T. Frauenheim, J. Phys. Chem. A **111**, 5678 (2007).
[32] E. Kirkland, *Advanced Computing in Electron Microscopy* (Plenum, New York, 1998).
[33] R. Egerton, P. Li, and M. Malac, Micron **35**, 399 (2004).
[34] R. Egerton, *Electron Energy-Loss Spectroscopy in the Electron Microscope* (Springer, New York, 1996).
[35] D. Taverna, M. Kociak, V. Charbois, and L. Henrard, Phys. Rev. B **66**, 235419 (2002).
[36] R. Arenal, O. Stéphan, M. Kociak, D. Taverna, A. Loiseau, and C. Colliex, Phys. Rev. Lett. **95**, 127601 (2005).
[37] E. Pop, D. Mann, Q. Wang, K. Goodson, and H. Dai, Nano Lett. **6**, 96 (2006).